First Cosmology Results using Type Ia Supernova from the Dark Energy Survey: Simulations to Correct Supernova Distance Biases

R. Kessler[1,2], D. Brout[3], C. B. D'Andrea[3], T. M. Davis[4], S. R. Hinton[4], A. G. Kim[5],
J. Lasker[1,2], C. Lidman[6], E. Macaulay[7], A. Möller[8,6], M. Sako[3], D. Scolnic[2], M. Smith[9],
M. Sullivan[9], B. Zhang[8,6], P. Andersen[4,10], J. Asorey[11], A. Avelino[12], J. Calcino[4], D. Carollo[13],
P. Challis[12], M. Childress[9], A. Clocchiatti[14], S. Crawford[15,16], A. V. Filippenko[17,18], R. J. Foley[19],
K. Glazebrook[20], J. K. Hoormann[4], E. Kasai[21,15], R. P. Kirshner[22,23], G. F. Lewis[24], K. S. Mandel[25],
M. March[3], E. Morganson[26], D. Muthukrishna[8,27,6], P. Nugent[5], Y.-C. Pan[28,29], N. E. Sommer[8,6],
E. Swann[7], R. C. Thomas[5], B. E. Tucker[8,6], S. A. Uddin[30], T. M. C. Abbott[31], S. Allam[32],
J. Annis[32], S. Avila[7], M. Banerji[27,33], K. Bechtol[34], E. Bertin[35,36], D. Brooks[37], E. Buckley-Geer[32],
D. L. Burke[38,39], A. Carnero Rosell[40,41], M. Carrasco Kind[42,26], J. Carretero[43], F. J. Castander[44,45],
M. Crocce[44,45], L. N. da Costa[41,46], C. Davis[38], J. De Vicente[40], S. Desai[47], H. T. Diehl[32], P. Doel[37],
T. F. Eifler[48,49], B. Flaugher[32], P. Fosalba[44,45], J. Frieman[32,2], J. García-Bellido[50], E. Gaztanaga[44,45],
D. W. Gerdes[51,52], D. Gruen[38,39], R. A. Gruendl[42,26], G. Gutierrez[32], W. G. Hartley[37,53],
D. L. Hollowood[19], K. Honscheid[54,55], D. J. James[56], M. W. G. Johnson[26], M. D. Johnson[26],
E. Krause[48], K. Kuehn[57], N. Kuropatkin[32], O. Lahav[37], T. S. Li[32,2], M. Lima[58,41], J. L. Marshall[59],
P. Martini[54,60], F. Menanteau[42,26], C. J. Miller[51,52], R. Miquel[61,43], B. Nord[32], A. A. Plazas[49],
A. Roodman[38,39], E. Sanchez[40], V. Scarpine[32], R. Schindler[39], M. Schubnell[52], S. Serrano[44,45],
I. Sevilla-Noarbe[40], M. Soares-Santos[62], F. Sobreira[63,41], E. Suchyta[64], G. Tarle[52], D. Thomas[7],
A. R. Walker[31], Y. Zhang[32]

(DES Collaboration)

Affiliations are in Appendix B.

ABSTRACT

We describe catalog-level simulations of Type Ia supernova (SN Ia) light curves in the Dark Energy Survey Supernova Program (DES-SN), and in low-redshift samples from the Center for Astrophysics (CfA) and the Carnegie Supernova Project (CSP). These simulations are used to model biases from selection effects and light curve analysis, and to determine bias corrections for SN Ia distance moduli that are used to measure cosmological parameters. To generate realistic light curves, the simulation uses a detailed SN Ia model, incorporates information from observations (PSF, sky noise, zero point), and uses summary information (e.g., detection efficiency vs. signal to noise ratio) based on 10,000 fake SN light curves whose fluxes were overlaid on images and processed with our analysis pipelines. The quality of the simulation is illustrated by predicting distributions observed in the data. Averaging within redshift bins, we find distance modulus biases up to 0.05 mag over the redshift ranges of the low-z and DES-SN samples. For individual events, particularly those with extreme red or blue color, distance biases can reach 0.4 mag. Therefore, accurately determining bias corrections is critical for precision measurements of cosmological parameters. Files used to make these corrections are available at `https://des.ncsa.illinois.edu/releases/sn`.

Key words: techniques – cosmology – supernovae

1 INTRODUCTION

Since the discovery of cosmic acceleration (Riess et al. 1998; Perlmutter et al. 1999) using a few dozen Type Ia supernovae (SNe Ia), surveys have been collecting larger SN Ia samples and improving the measurement precision of the dark energy equation of state parameter (w). This improvement is in large part due to the use of rolling surveys to discover and measure large numbers of SN Ia light curves in multiple passbands with the same instrument. The most recent Pantheon sample (Scolnic et al. 2018b) includes more than 1,000 spectroscopically confirmed SNe Ia from low and high redshift surveys. Compared to the 20th century sample used to discover cosmic acceleration, the Pantheon sample has more than a 20-fold increase in statistics and much higher quality light curves.

In addition to improving statistics and light curve quality, reducing systematic uncertainties is equally important. While most of the attention is on calibration, which is the largest source of systematic uncertainty, significant effort over more than a decade has gone into making robust simulations that are used to correct for the redshift-dependent distance-modulus bias (μ-bias) arising from selection effects. Selection effects include several sources of experimental inefficiencies: instrumental magnitude limits resulting in Malmquist bias, detection requirements from an image-subtraction pipeline used to discover transients, target selection for spectroscopic follow-up, and cosmology-analysis requirements. These selection effects introduce average μ-bias variations reaching ~ 0.05 mag at the high-redshift range of a survey. (e.g., see Fig. 5 in Betoule et al. (2014) and Fig. 6 in Scolnic et al. (2018b)), and the μ-bias averaged in specific color ranges can be an order of magnitude larger.

In addition to sample selection, the μ-bias depends on the parent populations of the SN Ia stretch and color, and also on intrinsic brightness variations, hereafter called 'intrinsic scatter,' in both the absolute magnitude and in the colors. For precision measurements of cosmological parameters, simulations are essential to determine μ-bias corrections, and these simulations require accurate models of SN light curves and sample selection.

The main focus of this paper is to describe our simulations of spectroscopically confirmed SNe Ia from three seasons of the Dark Energy Survey Supernova Program (DES-SN), and the associated low-z sample. The combination of these two samples, called DES-SN3YR, is used to measure cosmological parameters presented in DES Collaboration et al. (2019). All simulations were performed with the public "SuperNova ANAlysis" (SNANA) software package (Kessler et al. 2009a).[1] In addition to SNe Ia, a variety of source models can be supplied to the SNANA simulation, including core collapse (CC) SNe, kilonovae (KN), or any rest-frame model described by a time-dependent sequence of spectral energy distributions.

The SNANA simulations are performed at the "catalog level," which means that rather than simulating SN light curves on images, light curve fluxes and uncertainties are computed from image properties. The simulation inputs include a rest-frame source model, volumetric rate versus redshift, cosmological parameters (e.g., Ω_M, w), telescope trans-

mission in each passband, calibration reference, observing and image properties from a survey, and random numbers to generate Poisson fluctuations. The simulated light curves are treated like calibrated light curves from a survey, and are thus analyzed with the same software as for the data.

The SNANA simulation is ideally suited for rolling searches in which the same instrument is used for both discovery and for measuring light curves. Surveys with rolling searches include the Supernova Legacy Survey (SNLS; Astier et al. 2006), the Sloan Digital Sky Survey-II (SDSS-II; Frieman et al. 2008; Sako et al. 2018), the Panoramic Survey Telescope and Rapid Response System (PS1; Kaiser et al. 2002), and DES. The low-z sample, however, is based on follow-up observations from independent search programs (Hicken et al. 2009, 2012; Contreras et al. 2010; Folatelli et al. 2010, CFA, CSP), and the observing properties of the search are not available to perform a proper simulation. The low-z simulation, therefore, requires additional assumptions and approximations.

Simulated corrections first appeared in the SNLS cosmology analysis (Astier et al. 2006). Kessler et al. (2009b) analyzed several samples (low-z, SDSS-II, SNLS, ESSENCE), which led to a more general SNANA framework to simulate μ-bias corrections for arbitrary surveys. The heart of this framework is a set of two libraries. First, an observation library where each observation date includes a characterization of the point spread function (PSF), sky and readout noise, template noise, zero point, and gain. Second, a host-galaxy library includes magnitudes and surface profiles, and is used to compute Poisson noise and to model the local surface brightness. For a specified light curve model, these libraries are used to convert top-of-the-atmosphere model magnitudes into observed fluxes and uncertainties.

After a survey has completed, assembling the libraries is a relatively straightforward exercise, and SNANA simulations have been used in numerous cosmology analyses (Kessler et al. 2009b; Conley et al. 2011; Betoule et al. 2014; Rest et al. 2014; Scolnic et al. 2014b, 2018b). Before a survey has started, predicting the libraries is one of the critical tasks for making reliable forecasts. Such pre-survey forecasts with the SNANA simulation have been made for LSST[2] (LSST Science Collaboration et al. 2009; Kessler et al. 2010b), DES-SN (Bernstein et al. 2012), and WFIRST[3] (Hounsell et al. 2018).

While our main focus is to describe the DES-SN3YR simulation of SNe Ia, and how a large ($\sim 10^6$ events) simulated bias-correction sample is used to model biases in the measured distance modulus, it is worth noting other applications from the flexibility in SNANA. First, these simulations are used to generate 100 data-sized DES-SN3YR validation samples that are processed with the same bias corrections and cosmology analysis used on the data. This validation test is used to accurately check for w-biases at the ~ 0.01 level, and to compare the spread in w values with the fitted uncertainty (Brout et al. 2019b). The validation and bias-correction samples are generated with the same code and options, but are used for different tasks. Other applications include CC simulations for a classification challenge (Kessler

---

[1] https://snana.uchicago.edu

[2] Large Synoptic Survey Telescope: https://www.lsst.org
[3] Wide Field Infrared Space Telescope:
https://wfirst.gsfc.nasa.gov

et al. 2010a), CC simulations for a PS1 cosmology analysis using photometrically identified SNe Ia (Jones et al. 2017, 2018), simulating the KN search efficiency (Soares-Santos et al. 2016; Doctor et al. 2017), and making KN discovery predictions for 11 past, current, and future surveys (Scolnic et al. 2018a).

In this work we describe the simulation from a scientific perspective without instructions on implementation. For implementation, we refer to the manual available from the SNANA homepage, and recommend contacting community members familiar with the software. This simulation is possible because of extensive publicly available resources. When using this simulation in a publication, we recommend the added effort of referencing the relevant underlying contributions, such as the source of models or data samples used to make templates.

The organization of this paper is as follows. The DES-SN3YR sample is described in §2. An overview of the simulation method is in §3, and fake SN light curves overlaid on images is described in §4. Modeling is described in §5 for SNe Ia light curve magnitudes, §6 for fluxes and uncertainties, and §7 for the trigger. The quality of the simulation is illustrated with data/simulation comparisons in §8, and redshift-dependent μ-biases are described in §9. We conclude in §10, and present additional simulation features in the Appendix.

2 DATA SAMPLES

Here we describe the data samples that are simulated for the cosmology analysis in DES Collaboration et al. (2019) and Brout et al. (2019b). After selection, this sample includes 207 spectroscopically confirmed SNe Ia from the first three seasons (2013 August through 2016 February) of DES-SN (Diehl et al. 2016), and 122 low-z ($z < 0.1$) SNe Ia from CFA3 (Hicken et al. 2009), CFA4 (Hicken et al. 2012), and CSP (Contreras et al. 2010; Folatelli et al. 2010). This combined sample of 329 SNe Ia is called "DES-SN3YR."

The DES-SN sample was acquired in rolling search mode using the 570 Megapixel Dark Energy Camera (DECam; Flaugher et al. (2015)) mounted on the 4-m Blanco telescope at the Cerro Tololo Inter-American Observatory (CTIO). Ten 2.7 deg^2 fields were observed in g, r, i, z broadband filters, with a cadence of roughly 1 week in each band. Defining single-visit depth as the magnitude where the detection efficiency is 50%, eight of these fields have an average single-visit depth of ~ 23.5 mag (hereafter called 'shallow' fields), and the remaining two fields have a depth of ~ 24.5 mag (hereafter called 'deep' fields).

SNe Ia are detected by a difference-imaging pipeline (DiffImg) described in Kessler et al. (2015), and the spectroscopic selection is described in D'Andrea et al. (2018). The instrumental photometric precision from DiffImg is limited at the 2% level, and therefore a separate and more accurate "Scene Model Photometry (SMP)" pipeline (Brout et al. 2019a) is used to measure the light curve fluxes and uncertainties for the cosmology analysis. For each event, SMP simultaneously fits a 30×30 pixel-grid flux model to each observation, where the model includes a time-independent galaxy flux and a time-dependent source flux, each convolved with the PSF.

In addition to SN Ia light curves, the DES-SN data include other 'meta-data' for monitoring, calibration (e.g., telescope transmissions) and analysis. An important meta-data product for simulations is from the fluxes of $\sim 10,000$ 'fake' SN light curves overlaid on the images during the survey (§4), and processed in real time along with the data to find SN candidates with DiffImg.

The low-z sample includes redshifts, light-curve fluxes, flux uncertainties, and filter transmission functions. The photometry, however, is not from a rolling search but is from follow-up programs that target SNe Ia discovered from other search programs such as LOSS (Ganeshalingam et al. 2013). Since the observation information from the search programs is not available, the resulting observation library is an approximation based on several assumptions (§6.1.1).

3 OVERVIEW OF BIAS CORRECTIONS & SIMULATION

The primary goal of our simulation is to provide inputs to the 'BEAMS with Bias Correction' (BBC) method (Kessler & Scolnic 2017), which is the stage in our cosmology analysis that produces a bias-corrected SN Ia Hubble diagram (§3.8.1 of Brout et al. 2019b). A large simulated bias-correction sample is fit with the SALT-II light curve model, in the same way as for the data, to produce three parameters for each event: amplitude (x_0), stretch (x_1), and color (c). A statistical comparison of the fitted and true parameters is used to determine a bias correction for each parameter on a 5-dimensional (5D) grid of $\{z, x_1, c, \alpha, \beta\}$, where z is the redshift, x_1 and c are SALT-II-fitted parameters, and α and β are SALT-II standardization parameters (§5.3). BBC uses the 5D grid to bias-correct each set of SALT-II parameters from the data, and these corrected parameters are used to determine a bias-corrected distance modulus.

A schematic illustration of the SNANA simulation is shown in Fig. 1. The left column illustrates the generation of the source spectral energy distribution (SED), and astrophysical effects. These effects include host galaxy extinction, redshifting, cosmological dimming, lensing magnification, peculiar velocity, and Milky Way extinction. The output of this column is a true magnitude at the top of the atmosphere.

The middle column of Fig. 1 illustrates the instrumental simulation, where the true magnitude is converted into an observed number of CCD counts, hereafter denoted 'flux,' and the uncertainty on the flux. The observation information (PSF, sky noise, zero point) and host galaxy profile are used to compute the Poisson noise.

The right column in Fig. 1 illustrates the simulation of the trigger that selects events for analysis. Epochs that result in a detection, which is roughly a 5σ excess on the subtracted image (§7.1), are processed with additional logic to identify and store 'candidates' for analysis. The candidate logic specifies how many detections, from which band(s) the detection must occur, and the minimum time separation between detections. Finally, the trigger includes a selection function for the subset of candidates that were spectroscopically confirmed.

The noise and trigger models in Fig. 1 each have inputs

based on analyzing artificial light curves overlaid on CCD images. These fakes are described next in §4

4 FAKE SN IA LIGHT CURVES OVERLAID ON IMAGES

Ideally, simulated bias corrections would be based on SN Ia light curve fluxes overlaid onto CCD images and processed with exactly the same software as the data. The CPU resources for so many image-based simulations, however, would be enormous. Kessler et al. (2015) estimates that SNANA simulations are $\times 10^5$ faster than image-based simulations, while still producing realistic light curve fluxes and uncertainties. Although we do not perform image-based simulations for bias corrections, we use image simulations to inform the SNANA simulation. Specifically, 10,000 fake SN light curves were overlaid on DES-SN images and processed through the same pipelines as the data, including difference-imaging (DiffImg; Kessler et al. 2015) and photometry (Brout et al. 2019a) pipelines. For DiffImg, these fakes are used to measure the detection efficiency versus signal-to-noise ratio (SNR), which is needed for the trigger model in Fig. 1. For the photometry pipeline, fakes are used to measure the rms scatter between measured and true fluxes, and the rms is used to determine scale factors for the SN flux uncertainties (noise model in Fig. 1).

Prior to the start of DES operations, the fake light curve fluxes were computed from the SNANA simulation using the population of stretch and color (§5.1) from Kessler et al. (2013), and intrinsic scatter (§5.2) was ignored to simplify the analyses with fakes. The redshift distribution ($0.1 < z < 1.4$) is described by a polynomial function of redshift, and was tuned to acquire good statistics over the full redshift range and thus span the full range of SN magnitudes. Each fake location is selected on top of a random galaxy as described in §6.2. The SN model flux is distributed among pixels using the position-dependent PSF, and the flux in each pixel includes Poisson fluctuations from the sky background and the source.

The galaxy occupation fraction was limited to $\sim 1\%$ in each 0.05-wide redshift bin because the DES-SN search pipeline processed only one set of images, which included fakes, and a fake event overlaid on a galaxy prevents a real transient detection on that galaxy in the same season, but allows real events in future seasons where the fake is not overlaid. Once a real transient event is associated with a galaxy, fakes will not be overlaid on that galaxy. Since the SMP pipeline performs a global fit to all images, accurate astrometry is needed to overlay the fake light curve flux at the same sky location for each exposure. As described in Brout et al. (2019a), our astrometric precision results in $\sim$0.001 mag uncertainties for real sources, and thus the astrometric precision is adequate for the fakes.

Since the goal with fakes is to characterize single-epoch features of the CPU intensive image-processing pipelines, and to input these features into the much faster SNANA simulation, the choice of SN light curve model does not matter as long as the fake model magnitudes span the same range as the data. The resulting SNANA simulation can be used to simulate arbitrary light curve models and redshift dependence. For example, to evaluate systematic uncertainties in

this analysis, we simulate SNe Ia with different models of intrinsic scatter and with different populations of stretch and color.

While this seemingly large sample of SN fakes is used to characterize image-processing features, these fakes cannot be used to compute μ-bias corrections for two reasons. First, the light curve model used to generate fakes is deliberately different from reality for practical reasons explained above. Second, 10,000 fakes is more than an order of magnitude smaller than what is needed for the bias-correction sample used in the BBC method (Kessler & Scolnic 2017). In addition, even if an accurate SN Ia model were used to generate fakes, the resulting efficiency and bias corrections would be valid only for that particular SN Ia model, and not applicable to other SN Ia models, nor to transient models such as CC SNe or KNe.

5 SOURCE MODEL

Here we describe the simulation components under "Source Model" in Fig. 1. This includes the generation of the SN Ia SED as a function of time, how the SEDs are altered as the light travels from the source to Earth, and how each SED is transformed into a model magnitude above the atmosphere.

5.1 SN Ia Light Curve Model

To simulate SNe Ia, we use the SALT-II SED model described in Guy et al. (2010), and the trained model from the Joint Lightcurve Analysis (Betoule et al. 2014). The underlying model is a rest-frame SED with wavelengths spanning 2000 Å to 9200 Å, and rest-frame epochs spanning $-20 < T_{\rm rest} < +50$ days with respect to the epoch of peak brightness. For each event there are four SN-dependent parameters generated by the simulation:

(i) time of peak brightness, t_0, randomly selected between 2 months before the survey begins and one month after the survey ends.
(ii) SALT-II color parameter, c.
(iii) SALT-II stretch parameter, x_1.
(iv) CMB frame redshift, $z_{\rm cmb,true}$, selected from the rate model in §5.7 .

The rest-frame SED depends on the color and stretch parameters. For each epoch, the SED undergoes cosmological dimming (§5.4), is redshifted (§5.5) to the observer frame, and finally multiplied by the filter transmission function to produce generated fluxes and magnitudes. Wavelength-dependent Milky Way extinction (§5.6) is included in the flux-integrals, and thus the generated magnitudes are top-of-the-atmosphere. For epochs past 50 days, magnitudes are linearly extrapolated as a function of $T_{\rm rest}$. For light curve fitting we use epochs satisfying $-15 < T_{\rm rest} < 45$ days, but we simulate epochs outside this $T_{\rm rest}$ range to account for uncertainty in the fitted t_0, which increases the true $T_{\rm rest}$ range.

The SALT-II amplitude parameter, x_0, is computed using the estimator in Tripp (1998),

$$\log_{10}(x_0) = -0.4(\mu_{\rm model} + \mu_{\rm lens} - \alpha x_1 + \beta c - \mathcal{M}) , \quad (1)$$

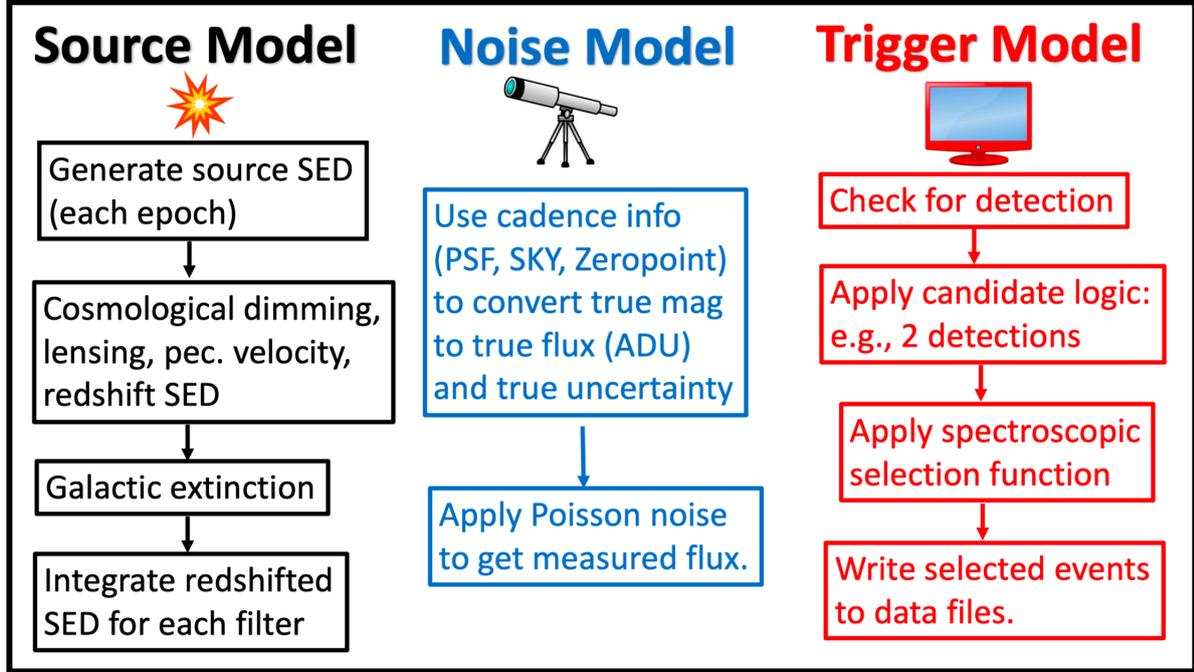where $\mu_{\rm model}$ is the distance modulus (§5.4) which depends

Figure 1. Flow chart of `SNANA` simulation.

on cosmology parameters, μ_{lens} is due to lensing magnification ($\S5.4$), α and β are SALT-II standardization parameters ($\S5.3$), and $\mathcal{M} = -19.365$ is a reference magnitude. It is well known that $\mathcal{M}$ is degenerate with the Hubble constant (H_0), and that their values have no impact in the SN Ia analysis of cosmological parameters. However, the quality of the simulation depends on predicting accurate observer-frame magnitudes, and therefore $\mathcal{M} + 5\log_{10}(H_0)$ must be well determined. The SALT-II SED is redshifted using the heliocentric redshift ($z_{\mathrm{hel,true}}$), which is transformed from $z_{\mathrm{cmb,true}}$ using the sky coordinates from the observation library. $z_{\mathrm{hel,true}}$ also includes a random host-galaxy peculiar velocity described in $\S5.5$.

5.2   Intrinsic Scatter

Before redshifting the SALT-II SED, intrinsic scatter is applied as spectral variations to the SED. To evaluate systematic uncertainties in the bias corrections, two different models are used that approximately span the range of possibilities in current data samples. First is the 'G10' model (Guy et al. 2010) from the SALT-II training process. Roughly 75% of the scatter is coherent among all wavelengths and epochs, while the remaining 25% of the scatter results from color variations that are not correlated with luminosity. The second model, 'C11,' is based on broadband ($UBVRI$) co-variances found in Chotard et al. (2011). Only 25% of the scatter is coherent, while the remaining scatter results from color variations. Details of these models are given in Kessler

et al. (2013), and both models result in 0.13 mag intrinsic scatter on the Hubble diagram.[4]

5.3   **Global** SALT-II **Model Parameters**

While the SALT-II SED and color law model parameters from the training process are fixed for each SN, there are a few parameters that are determined outside the training process. To simulate validation data samples, the standardization parameters are: $\alpha = 0.15$, $\beta_{\mathrm{G10}} = 3.1$, and $\beta_{\mathrm{C11}} = 3.8$, where G10 and C11 refer to the intrinsic scatter model ($\S5.2$). The standardization parameters for the μ-bias simulations are defined on a 2×2 grid to enable BBC interpolation of the μ-bias as a function of α and β; this is described in $\S9$.

For the population of stretch (x_1) and color (c), we use the asymmetric Gaussian parametrization from Scolnic & Kessler (2016, hereafter SK16). For DES-SN stretch & color, we use the high-z G10 and C11 rows from Table 1 of SK16. For the low-z sample we use the color population parameters from the low-z row of Table 1 of SK16. The stretch population is double-peaked, and we use the parametrization from Appendix C of Scolnic et al. (2018b). While we account for the color and stretch population differences between low-z and DES-SN, the redshift dependence of the population

---

[4] This 0.13 mag scatter is larger than typical fitted σ_{int} values of 0.1 mag because of SALT-II model uncertainties; see $\S$ 7.1 of Kessler & Scolnic (2017) for explanation.

has not been quantified and therefore is not included in our simulations.

5.4   Luminosity Distance and Lensing Magnification

The luminosity distance (D_L) for a flat universe is computed as

$$D_L = (1 + z_{\rm hel,true})\frac{c}{H_0}\int_0^{z_{\rm cmb,true}} dz/E(z) \quad (2)$$

$$E(z) = \left[\Omega_\Lambda (1+z)^{3(1+w)} + \Omega_{\rm M}(1+z)^3\right]^{1/2} ,$$

where $\Omega_{\rm M}$ is today's matter density, Ω_Λ is today's dark energy density, and w is the dark energy equation of state parameter. Note that both the CMB and heliocentric redshifts are used to compute D_L, but the $1 + z_{\rm hel,true}$ pre-factor is an approximation: the exact pre-factor is $1 + z_{\rm obs}$, where $z_{\rm obs}$ is the measured redshift (Davis et al. 2011). However, we do not simulate Earth's motion around our Sun, nor the local SN motion within its host galaxy, and therefore $z_{\rm obs} = z_{\rm hel,true}$. The error on D_L from ignoring local motions is less than 10^{-3}. To compute $E(z)$ in our simulations we set $H_0 = 70$ km/s,[5] $\Omega_\Lambda = 0.7$, $\Omega_{\rm M} = 0.3$ and $w = -1$. The distance modulus ($\mu_{\rm model}$ in Eq. 1) is defined as $\mu_{\rm model} = 5\log_{10}(D_L/10 \text{ pc})$.

Weak lensing effects are described by the $\mu_{\rm lens}$ term in Eq. 1, and modeled as follows:

• $0.4 < z < 1.4$: A convergence (κ) distribution is determined from a 900 deg^2 patch of the MICECAT N-body simulation (Crocce et al. 2015).[6] Galaxies are from a halo occupation distribution and a sub-halo abundance matching technique (Carretero et al. 2015). The lensing distribution is determined from $\mu_{\rm lens} = 5\log_{10}(1-\kappa)$ (shear contribution is negligible and ignored).

• $z < 0.4$: Using the MICECAT approach above to determine $\mu_{\rm lens}$ at $z = 0.4$ ($\mu_{\rm lens,0.4}$), the lensing at lower redshifts is computed as

$$\mu_{\rm lens,z} = \mu_{\rm lens,0.4} \times z/0.4 . \quad (3)$$

As a crosscheck, this z-scale approximation works well within the MICECAT redshift range: e.g., $\mu_{\rm lens,0.4} \simeq \mu_{\rm lens,0.6} \times (0.4/0.6)$.

The root mean square (rms) scatter in the model $\mu_{\rm lens}$ distribution is approximately $0.05 \times z$. For systematic studies, the simulation includes an option to scale the width of the distribution to increase or decrease the scatter.

To properly select from the asymmetric $\mu_{\rm lens}$ distribution, instead of a Gaussian approximation, the lensing magnification probability is defined as a 2-dimensional function of redshift and $\mu_{\rm lens}$. For each simulated redshift, a random $\mu_{\rm lens}$ is selected from the $\mu_{\rm lens}$ probability distribution. While our lensing model accounts for large scale structure on average, it does not account for correlations between events with small angular separations.

---

[5] This H_0 value was used in the SN Ia model training, which determines the absolute brightness $\mathcal{M}$, and therefore the simulated H_0 should not be updated with more recent measurements.
[6] https://cosmohub.pic.es

5.5   Peculiar Velocity and Observed Redshift

The generated CMB-frame redshift, $z_{\rm cmb,true}$, is transformed to the heliocentric frame, $z_{\rm hel,true}$, using the sky coordinates from the observation library. The redshift observed in the heliocentric frame is

$$\begin{aligned}z_{\rm hel,obs} &= (1 + z_{\rm hel,true})(1 + v_{\rm pec}/c - v_{\rm pec,cor}/c) - 1 (4)\\ &\quad + \delta z_{\rm noise}\\ &= (1 + z_{\rm hel,true})(1 - v_{\rm pec,err}/c) - 1 \quad (5)\\ &\quad + \delta z_{\rm noise} ,\end{aligned}$$

where $v_{\rm pec}$ is a peculiar velocity randomly chosen from a Gaussian profile with $\sigma_{\rm vpec} = 300$ km/sec, and $\delta z_{\rm noise}$ is a measurement error. For DES-SN and low-z, $\delta z_{\rm noise}$ is drawn from a Gaussian with $\sigma_z = 10^{-4}$.

While the peculiar velocity model is the same for low-z and DES-SN, corrections are modeled only for the low-z sample. The simulated low-z correction simply reduces the $v_{\rm pec}$ scatter without applying real corrections. Following the Pantheon analysis (Scolnic et al. 2018b), $v_{\rm pec,cor} = v_{\rm pec} + v_{\rm pec,err}$ where $v_{\rm pec,err}$ is a randomly selected error from a Gaussian profile with a 250 km/sec sigma. Finally, $z_{\rm hel,obs}$ is transformed back to the CMB frame redshift, $z_{\rm cmb,obs}$. Peculiar velocity corrections for DES-SN can be computed in principle, but such corrections on a high-redshift sample are negligible and were thus ignored.

5.6   Galactic Extinction

For each simulated event the Galactic extinction parameter, $E(B - V)$, is computed from the maps in Schlegel et al. (1998). Following a stellar analysis from SDSS (Schlafly & Finkbeiner 2011), we scale the $E(B - V)$ values by 0.86. We assume the reddening law derived in Fitzpatrick (1999), and with A_V defined as the extinction at 5500 Å, $R_V \equiv A_V/E(B - V) = 3.1$.

5.7   Volumetric Rate Model

The redshift distribution of SNe Ia is generated from a comoving volumetric rate, $R(z)$, measured by SNLS (Perrett et al. 2012):

$$R(z) = 1.75 \times 10^{-5}(1+z)^{2.11} \text{ yr}^{-1}\text{Mpc}^{-3} , \quad (6)$$

and is valid up to redshift $z < 1$.

6   MODELING FLUX AND NOISE

Here we describe the simulation components under 'Noise Model' in Fig. 1. There are two steps needed to simulate flux and noise. First, an observation library is needed to characterize observing conditions (§6.1). Next, each true model magnitude is converted into a measured flux (CCD counts) and uncertainty (§6.3).

6.1   Observation Library

An observation library is a collection of sky locations, each specified by right ascension (RA) and declination (Dec), along with a list of observations for each location. For a

small survey area, a single sky location may be adequate, particularly for making forecasts. For a proper simulation, however, many sky locations should be used with either random sampling or a grid. For DES-SN we use $\sim 10^4$ random sky locations covering 27 deg^2, which averages over density fluctuations to achieve a representative sample for a homogeneous universe. For simulations with more than 10^4 generated events, the library sky locations and observations are re-used with SNe that have a different set of randomly chosen properties. Since $\sim 1\%$ of the DES-SN events occur in the overlap between two adjacent fields, and thus have double the number of observations, the simulation includes a mechanism to handle overlapping fields.

The exposure information for each sky location is defined as follows:

- `MJD` is the modified Julian date.
- `FILTER` is the filter passband.
- `GAIN` is the number of photoelectrons per ADU[7].
- `SKYSIG` is the sky noise, including read noise.
- $\sigma_{\text{PSF}} = \sqrt{\text{NEA}/4\pi}$ is an effective Gaussian σ for the PSF, and `NEA` is the noise-equivalent area defined as

$$\text{NEA} = \left[2\pi \int [\text{PSF}(r)]^2 r\, dr \right]^{-1}. \qquad (7)$$

For a PSF-fitted flux, the fitted flux variance is the sky noise per pixel multiplied by `NEA`.

- `ZPTADU` is the zero point (ADU), and includes telescope and atmospheric transmission.

Many of the DES-SN visits include multiple exposures: two z-band exposures in each of the 8 shallow fields,[8] and the 2 deep fields include 3, 3, 5, 11 exposures for g, r, i, z-bands, respectively. During the survey, `DiffImg` performs the search on co-added exposures. In the analysis, `SMP` determines the flux for each individual exposure, and the fluxes are co-added at the catalog level. The co-adding for both `DiffImg` and `SMP` are treated the same in the simulation by co-adding the observation library information as follows:

$$
\begin{aligned}
\text{MJD} &= \left[\sum \text{MJD}_i \right] / N_{\text{expose}} \\
\text{SKYSIG} &= \sqrt{\sum \text{SKYSIG}_i^2} \\
\sigma_{\text{PSF}} &= \left[\sum \sigma_{\text{PSF}\,i} \right] / N_{\text{expose}} \\
\text{ZPTADU} &= 2.5 \times \log_{10} \left[\sum 10^{(0.4 \cdot \text{ZPTADU}_i)} \right],
\end{aligned} \qquad (8)
$$

where N_{expose} is the number of exposures and each sum includes $i = 1, N_{\text{expose}}$. `ZPTADU` is an approximation assuming the same `GAIN` for each exposure; the DES `GAIN` variations are a few percent.

The randomly selected time of peak brightness (t_0, §5.1), along with the light-curve time window, determine the `MJD`-overlap in the observation sequence.

6.1.1   *Observation Library for Low-z Sample*

The low-z sample does not include the observation properties (PSF, sky noise, zero point) from their image-processing pipelines. Therefore we construct an approximate library from the low-z light curves, using their sky locations, observation dates, and SNR. There is not enough light curve information to uniquely determine the observation properties, and therefore we use three assumptions: (1) fix each `GAIN` to unity, (2) fix each PSF to $1''$ (FWHM), and (3) use a previously determined set of broadband sky magnitudes, and interpolate the sky magnitude to the central wavelength of each simulated filter. For ground-based surveys we use the average sky mags in $ugrizY$ passbands from a simulation of LSST (Delgado et al. 2014). The `ZPTADU` parameter is adjusted numerically so that the calculated SNR matches the observed SNR.

Another subtlety is that the low-z sample was collected over decades, and thus for a randomly selected explosion time there is little chance that the simulated light curve would overlap the observation dates. To generate low-z light curves more efficiently, the measured time of peak brightness (t_0) for each light curve is used for the corresponding sky location, thus ensuring a light curve will be generated. Other SN properties (redshift, color, stretch, intrinsic scatter) are randomly selected in the same way as for the DES-SN simulation.

6.2   Host Galaxy Model

Host galaxies are used for two purposes in the `SNANA` simulations of DES-SN. First, fakes are generated to be overlaid on top of galaxies in real CCD images. Second, to simulate bias corrections and validation samples in the analysis, the local surface brightness from the host is used to add Poisson noise and anomalous scatter (Fig. 2) in the light curve fluxes. We do not simulate low-z host galaxies because the cadence library is constructed from observed SNR that should already include Poisson noise from the host. While anomalous scatter in the low-z sample may be present, the local surface brightness information is not available to study this effect.[9]

For DES-SN the `SNANA` simulation uses a host galaxy library (`HOSTLIB`), where each galaxy is described by (1) heliocentric redshift, $z_{\text{HOST,hel}}$, (2) coordinates of the galaxy center, (3) observer-frame magnitudes in the survey bandpasses, and (4) Sérsic profile with index $n = 0.5$ (Gaussian), and half-light radii along the major and semi-major axes. The `HOSTLIB` can be created from data or from an astrophysical simulation. Our DES-SN simulation uses a galaxy catalog derived from the DES science verification (SV) data, as described in Gupta et al. (2016). Eventually this galaxy catalog will be updated using a much deeper co-add from the full DES data set.

There are two caveats about this `HOSTLIB`. First, $z_{\text{HOST,hel}}$ are photometric redshifts (photo-z). Extreme photo-z outliers are rejected by requiring the absolute r and i band magnitudes ($M_{r,i}$) to satisfy $-23 < M_{r,i} < -16$, where $M_{r,i} = m_{r,i} - \mu_{\text{phot}}$, $m_{r,i}$ are the observed magnitudes, and

---

[7] ADU: Analog to Digital Unit.
[8] shallow g, r, i include one exposure per visit.

[9] It would be a valuable community contribution to use public survey data (e.g., PS1, SDSS, DES) and determine the local surface brightness for each low-z event.

$\mu_{\rm phot}$ is the distance modulus computed from the photo-z. The second caveat is that the measured half-light radii were scaled by a factor of 0.8 to obtain better data-simulation agreement in the surface brightness distribution (§8).

To generate fakes to overlay on images, each SN was associated with a random `HOSTLIB` event satisfying

$$|z_{\rm SN,hel} - z_{\rm HOST,hel}| < 0.01 + 0.05 z_{\rm SN} , \qquad (9)$$

where $z_{\rm SN,hel}$ and $z_{\rm HOST,hel}$ are the heliocentric redshifts for the SN and host galaxy, respectively. The SN redshift is updated to $z_{\rm HOST,hel}$, the CMB-frame redshift ($z_{\rm cmb,true}$) is computed from $z_{\rm HOST,hel}$, and the resulting $z_{\rm cmb,true}$ is used to update the distance modulus and light curve magnitudes. To avoid multiple fakes around a single galaxy, each `HOSTLIB` event can be used only once. The SN coordinates are chosen near the host, weighted by the Sérsic profile.

To simulate samples for the analysis, the redshift matching between the SN and the host is the same as for fakes (Eq. 9). However, the generated SN redshift (from rate model) and its coordinates (from cadence library) are preserved. A random location near the host is selected from the Sérsic profile, and is used to determine the local surface brightness and to add Poisson noise to the light curves. The Poisson noise variance is computed by integrating the host-galaxy flux over the noise equivalent area (Eq. 7). In this implementation of the DES-SN simulation, the host-galaxy spatial distribution is homogeneous on all scales. Large-scale structure can be incorporated as explained in the Appendix.

6.3   Converting True Magnitudes into Measured Fluxes & Uncertainties

Here we describe how a true source magnitude at the top of the atmosphere, $m_{\rm true}$, is used to determine the instrumental flux and its uncertainty. The flux unit for this discussion is photoelectrons, but the simulation uses the `GAIN` to properly digitize the signals in ADU.

The true flux is given by

$$F_{\rm true} = 10^{0.4(m_{\rm true} - {\rm ZPTpe})} , \qquad (10)$$

where ${\rm ZPTpe} = {\rm ZPTADU} + 2.5 \log_{10}({\rm GAIN})$ is the zero point in units of photoelectrons.

The true Poisson noise for the measured flux is given by

$$\sigma_{\rm Ftrue}^2 = [F_{\rm true} + ({\rm NEA} \cdot b) + \sigma_{\rm host}^2] \hat{S}_{\rm sim}^2 , \qquad (11)$$

where

- $F_{\rm true}$ is the true flux;
- `NEA` is the noise equivalent area (Eq. 7);
- b is the background per unit area (includes sky and CCD read noise);
- $\sigma_{\rm host}$ is Poisson noise from the underlying host galaxy (§6.2);
- $\hat{S}_{\rm sim}$ is an empirically determined scale (§6.4) that increases both the flux scatter and measured uncertainty.

`NEA`, b, and $\sigma_{\rm PSF}$ are obtained from the observation library (§6.1). $\hat{S}_{\rm sim}$ is determined from analyzing the fakes (§6.4), and characterizes subtle scene model photometry (`SMP`) behavior that cannot be computed from first principles, mainly the anomalous flux scatter from bright galaxies. Because of the large number of reference images used in `SMP`, we do not include an explicit template noise term.

For PSF-fitted fluxes, the noise estimate in Eq. 11 is an approximation that is more accurate for sky-dominated noise, or as $F_{\rm true}/({\rm NEA} \cdot b)$ becomes smaller. In principle Eq. 11 is also accurate for bright events with high SNR, but brighter SNe are associated with brighter galaxies that introduce anomalous flux scatter. In §6.4 below, we use fakes to show how the simulated flux uncertainties are corrected for anomalous scatter so that the uncertainties are accurate over the full range of SNR.

The true uncertainty ($\sigma_{\rm Ftrue}$) is used to select a random fluctuation on the true flux ($F_{\rm true}$), resulting in the observed flux, F. The measured uncertainty for data is not the true uncertainty, but rather an approximation based on the observed flux. In the simulation, the measured uncertainty, σ_F, is computed from the observed flux by substituting $F_{\rm true} \rightarrow F$ in Eq. 11:

$$\sigma_F = \sqrt{\sigma_{\rm Ftrue}^2 + (F - F_{\rm true})} \quad (F > 0) , \qquad (12)$$

$$\sigma_F = \sqrt{\sigma_{\rm Ftrue}^2 - F_{\rm true}} \qquad (F < 0) . \qquad (13)$$

In the case where $F < 0$ due to a sky noise fluctuation, the measured uncertainty is not reduced (relative to $F = 0$) because σ_F is dominated by sky noise which is determined from a CCD region well away from the SN.

6.4   Determining The Flux-Uncertainty Scale ($\hat{S}_{\rm sim}$)

An accurate description of the uncertainty is important in order to model selection cuts on quantities related to SNR and chi-squared from light curve fitting. With $\hat{S}_{\rm sim} = 1$, the calculated flux uncertainty, $\sigma_{\rm Ftrue}$ in Eq. 11, is an approximation for PSF-fitting, and it does not account for all of the details in the `SMP` pipeline. We correct the simulated uncertainty to match the observed flux scatter in the fakes, which we interpret to be the true scatter in the data. The uncertainty correction, $\hat{S}_{\rm sim}$, is defined as

$$\hat{S}_{\rm sim}(\vec{\mathcal{O}}) = \frac{{\rm rms}[(F_{\rm true} - F_{\rm SMP})/\sigma_F']_{\rm fake}}{{\rm rms}[(F_{\rm true} - F_{\rm sim})/\sigma_F']_{\rm sim}} , \qquad (14)$$

where $F_{\rm true}$ is the true flux, $F_{\rm SMP}$ is the fake flux determined by `SMP`, and $F_{\rm sim} = F_{\rm true} + \mathcal{N}(0, \sigma_F)$ is the simulated flux with $\hat{S}_{\rm sim} = 1$.

The σ_F' term in both denominators is a common reference so that the $\Delta F/\sigma_F'$ ratios in Eq. 14 are $\sim$unity, which significantly improves the sensitivity in measuring the $\hat{S}_{\rm sim}$ map. σ_F' is the naively expected uncertainty computed from Eq. 11 with $\hat{S}_{\rm sim} = 1$, $F_{\rm true} \rightarrow F$, and $\sigma_{\rm host}$ computed using the approximation of a constant local surface brightness magnitude over the entire noise-equivalent area. This $\sigma_{\rm host}$ approximation can be used with photometry that does not include a detailed model of the host galaxy profile, and simulation tests have shown that this approximation does not degrade the determination of $\hat{S}_{\rm sim}(\vec{\mathcal{O}})$.

The numerator includes information from the fakes and `SMP` pipeline. The argument $\vec{\mathcal{O}}$ indicates an arbitrary dependence on observed image properties. For the DES-SN3YR analysis we use a 1-dimensional map with $\vec{\mathcal{O}} = \{m_{\rm SB}\}$, where $m_{\rm SB}$ is the local surface brightness magnitude. Before determining $\hat{S}_{\rm sim}$, it is important that the simulated distributions in redshift, color, and stretch (§5.1) are tuned to
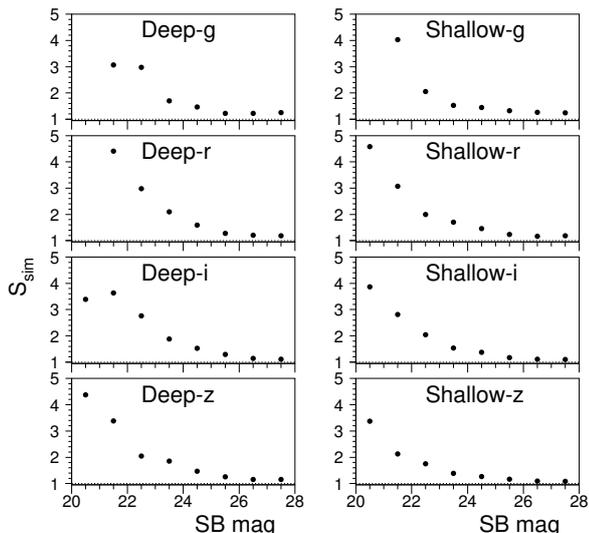
Figure 2. Simulated uncertainty scale, $\hat{S}_{\rm sim}$, as a function of local surface brightness mag (SB mag). Each panel indicates the set of fields and passband. Left panels are for the deep SN fields (depth per visit ~ 24.5); right panels are for shallow SN fields (depth per visit ~ 23.5).
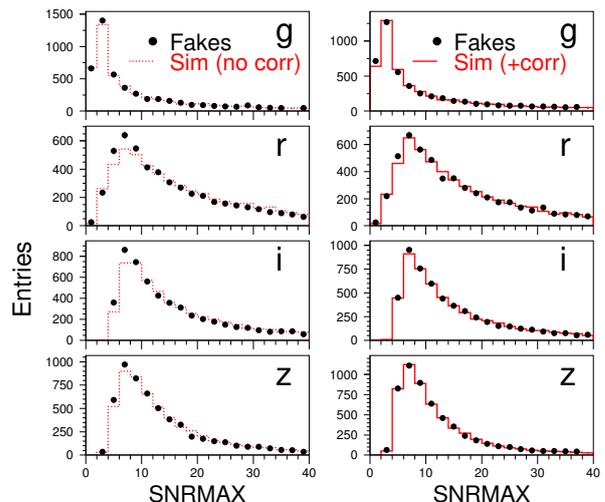

Figure 3. Distribution of maximum SNR in the DES band labeled on each panel. Filled circles are for the fakes processed through the SMP pipeline; histogram is the simulation. Left panels are before applying the $\hat{S}_{\rm sim}$ scale; right panels are after applying the $\hat{S}_{\rm sim}$ scale from Fig. 2.

match the distributions for the fakes. After this tuning, $\hat{S}_{\rm sim}$ versus $m_{\rm SB}$ is shown in Fig. 2. For $m_{\rm SB}$ values outside the defined range of the map, $\hat{S}_{\rm sim}$ is computed from the closest $m_{\rm SB}$ value in the map. This $m_{\rm SB}$-dependence has been seen previously in the difference-imaging pipeline (Kessler et al. 2015; Doctor et al. 2017), and it persists in the SMP photometry. After applying the corrections in Fig. 2, the flux uncertainties for the fakes and simulations agree to within 5% over the entire $m_{\rm SB}$ range.

The impact of the uncertainty corrections is shown in Fig. 3, which compares the maximum SNR distribution in each band for fakes and the simulation. Compared to simulations with no correction, simulations with corrections show much better agreement with the fakes.

While Eq. 14 describes the simulated correction, there is an analogous correction for the data uncertainty produced by SMP: $\sigma_{\rm SMP} \rightarrow \sigma_{\rm SMP} \times \hat{S}_{\rm SMP}$, where

$$\hat{S}_{\rm SMP}(\vec{\mathcal{O}}) = \frac{{\rm rms}[(F_{\rm true} - F_{\rm SMP})/\sigma'_F]_{\rm fake}}{\langle \sigma_{\rm SMP}/\sigma'_F \rangle_{\rm fake}} \ . \qquad (15)$$

The observed scatter in the fakes is a common reference for both the data and simulations, and therefore the numerator (Eq. 15) is the same as for the simulated correction (Eq. 14). The denominator, $\langle \sigma_{\rm SMP}/\sigma'_F \rangle_{\rm fake}$, specifies an average within each $\vec{\mathcal{O}}$ bin. This $\hat{S}_{\rm SMP}$ correction is applied to the data uncertainties, including fakes, while $\hat{S}_{\rm sim}$ is applied to the simulated noise and uncertainty. More details of $\hat{S}_{\rm SMP}$ are given in Brout et al. (2019a).

7 TRIGGER MODEL

Here we describe the simulation components under 'Trigger Model' in Fig. 1. Ideally, every DECam pixel would be continuously monitored for transient activity. However, storing light curves near every pixel is impractical with today's

computing, and therefore a 'trigger' is used to select candidates for analysis. Here we describe the trigger simulation for the DES-SN and low-z samples. For a general survey, the simulation of the trigger consists of three stages: 1) detecting PSF-shaped objects above threshold, 2) matching multiple objects, from different bands and nights, to form candidates, and 3) selection for spectroscopic classification. All three stages are modeled for DES-SN. For low-z, however, we do not have information to simulate the first two trigger stages and therefore all three trigger stages are empirically combined in the third stage.

The total efficiency ($E_{\rm TOT}$) can be described by

$$E_{\rm TOT} = E_{\rm S\vec{N}R} \times E_{\rm spec} \ , \qquad (16)$$

where $E_{\rm S\vec{N}R}$ includes the first two trigger stages and depends on the SNR for each epoch ($\rm S\vec{N}R$), and $E_{\rm spec}$ describes the spectroscopic selection in the third stage. We do not explicitly define $E_{\rm S\vec{N}R}$, but instead model the efficiency vs. SNR for each epoch. $E_{\rm spec}$, however, is explicitly described by a smooth function of magnitude at peak brightness. Another subtlety here is that $E_{\rm S\vec{N}R}$ is valid for arbitrary transient source models, while $E_{\rm spec}$ is valid only for SNe Ia and only if the first two trigger stages are satisfied.

7.1 DES-SN Trigger

For the first trigger stage, fakes are used to characterize the detection efficiency versus SNR in each filter, as shown in Fig. 8 of Kessler et al. (2015). The efficiency reaches 50% around SNR~ 5. Since these efficiency curves are intended for simulations, we do not use the measured SNR, but instead the fake SNR is calculated from the true flux (Eq. 10) and noise (Eq. 11) with $\hat{S}_{\rm sim} = 1$. These efficiency curves are therefore determined as a function of a calculated SNR quantity that is calculated in exactly the same way in the simulation.

In the second trigger stage, a candidate requires two

detections on separate nights within 30 days. Thus a single-night detection in all four bands (g, r, i, z) will not trigger a candidate. However, a single-band detection on two separate nights will trigger a candidate.

The third trigger stage, spectroscopic selection efficiency (E_{spec}), is the most subtle. While the selection algorithm was designed to exclude human decisions as much as possible (D'Andrea et al. 2018), we are not able to simulate the selection algorithm because we have eight frequently used telescopes, inefficiencies due to weather and scheduling, spectral classification uncertainty, and a small amount of human decision making.

Ideally we would compute E_{spec} as a ratio of spectroscopically confirmed events (numerator) to photometrically identified events (denominator). A data-derived E_{spec} analysis is under development and described in D'Andrea et al. (2018), but here we use simulations to predict the denominator. A caveat is that a simulation used to determine E_{spec} needs the population parameters for stretch and color (§5.3), which is determined from simulations that already include E_{spec}. Rather than performing an iterative procedure with DES-SN data, we use the population parameters from external data sets as described in SK16, who show that varying the external E_{spec} functions has a negligible effect on the population parameters.

Without a well-defined algorithm to compute E_{spec}, we use an empirical model where E_{spec} depends on the i-band magnitude at the epoch of peak brightness, i_{peak}. The basic idea is to compare the i_{peak} distribution between data and a simulated sample passing the first two trigger stages (i.e., with $E_{spec} = 1$). We define $E_{spec}(i_{peak})$ to be a smooth curve fit to the data/sim ratio as a function of i_{peak} (solid curve in Fig. 4), where i_{peak} is computed from the best-fit SALT-II model. The data/sim ratio is fit to a sigmoid function,

$$E_{spec}(i_{peak}) = s_0[1 + e^{(s_1 i_{peak} - s_2)}]^{-1} , \qquad (17)$$

where s_0, s_1, s_2 are floated parameters determined with `emcee` (Foreman-Mackey et al. 2013) and the data uncertainties are modeled using a Poisson distribution. For the cosmology analysis, E_{spec} can be arbitrarily scaled (bounded between 0 and 1) without affecting the μ-bias determination, and thus to generate events most efficiently we have scaled E_{spec} to have a maximum efficiency of 1.

There is a subtle caveat in the `DiffImg` trigger modeling related to bright galaxies. As illustrated in Figure 7 of Doctor et al. (2017), image-subtraction artifacts result in an anomalous decrease in detection efficiency as the local surface brightness increases. Here the term 'anomalous' indicates an efficiency loss that is much greater than expected from the increased Poisson noise from the host galaxy. While Fig. 2 shows how the `SNANA` simulation models anomalous scatter, the simulation does not model the anomalous detection inefficiency. Studies with fakes have shown that this bright-galaxy anomaly does not reduce the trigger efficiency for nearby SNe Ia on bright galaxies. The reason is that there are a few dozen opportunities to acquire detections, and it is very unlikely to fail the 2-detection trigger requirement.

7.2   Low-z Trigger

As explained in Betoule et al. (2014) and Scolnic et al. (2014b), there is evidence that the low-z search is magni-
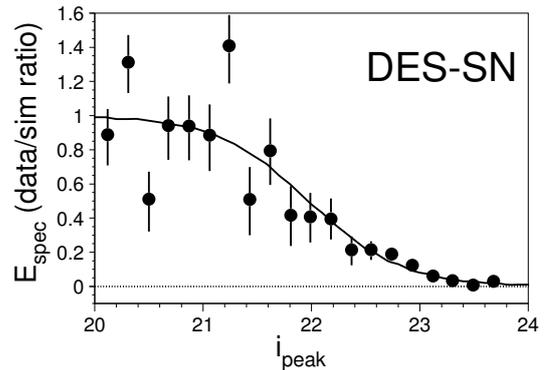

Figure 4. E_{spec} vs. i_{peak} for DES-SN sample. Filled circles are data/sim ratios, with error bars from Poisson uncertainties on the best-fit model curve. The simulation includes the first two trigger stages ($E_{spec} = 1$), uses the G10 scatter model, and is scaled to match the data statistics for the brightest events. Smooth solid curve is a fit that defines E_{spec} in the simulation, and max $E_{spec} = 1$ is an arbitrary normalization.
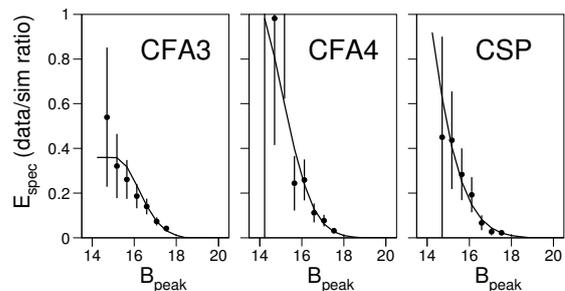

Figure 5. E_{spec} vs. B_{peak} for each low-z sample. Filled circles are the data/sim ratio with $E_{spec} = 1$ in the simulation. Smooth curve is a fit that defines E_{spec} in the simulation.

tude limited because of the decreasing number of events with redshift, and because higher redshift events are bluer. On the other hand, many low-z searches target a specific list of galaxies, suggesting a volume-limited sample. We therefore simulate both assumptions for evaluating systematic uncertainties.

For the magnitude-limited assumption, we incorporate all trigger stages into a single E_{spec} function of B-band magnitude at the time of peak brightness (B_{peak}). Following the recipe for the DES-SN simulation, we simulate a low-z sample with $E_{\vec{SNR}} = 1$ and define E_{spec} to be the data/sim ratio vs. B_{peak} (Fig. 5). The fitted B_{peak} function is a one-sided Gaussian as described in Appendix C of Scolnic et al. (2018b). Describing E_{spec} as a function of V or R band also works well, so the choice of B band is arbitrary.

For the volume-limited assumption, which is used as a systematic uncertainty in Brout et al. (2019b), we set $E_{TOT} = 1$ and interpret the redshift evolution of stretch and color to be astrophysical effects instead of artifacts from Malmquist bias. To match the low-z data, the low-z simulation is tuned using redshift-dependent stretch and color populations: $x_1 \rightarrow x_1 + 25z$ and $c \rightarrow c - 1z$. There is no physical motivation for this redshift dependence, and therefore this is a conservative assumption for the systematic uncertainty.

8 COMPARING DATA & SIMULATIONS

Here we qualitatively validate the simulations by comparing simulated distributions with data. While we do not quantify the data-simulation agreement here (e.g., via χ^2), such quantitative comparisons are used to assess systematic uncertainties in Brout et al. (2019b). To limit statistical uncertainties in these comparisons, very large simulations are generated and the distributions are scaled to match the statistics of the data. Recall that the tuned distributions are $E_{\rm spec}(i_{\rm peak})$ and the populations for stretch and color; all other inputs to the simulation are from measurements.

We apply light-curve fitting and selection requirements (cuts) that depend on SALT-II fitted parameters, SNR, and light curve sampling (§3.5 of Brout et al. 2019b). After applying these cuts, data/simulation comparisons for DES-SN are shown in Fig. 6. The $i_{\rm peak}$ distribution for data and simulation are guaranteed to match because of the method for determining $E_{\rm spec}$ in §7.1. The redshift agreement is not enforced, but is still excellent. The next two distributions, $E(B-V)$ and maximum gap between observations, are also in excellent agreement, and this agreement validates the choice of random sky locations in the cadence library. The double peak structure of $E(B-V)$ is from the large sky separations between groups of fields.

The middle column of Fig. 6 compares the maximum SNR in each band, and these are the most difficult distributions to predict with the simulation. The comparisons look good, except for a slight excess in the simulation for $\mathrm{SNR} > 100$. The right column of Fig. 6 compares the local surface brightness mag in each band. There is good agreement in all bands for $\mathrm{SB} < 24$, For fainter hosts beyond the detection limit the agreement is much poorer, and is likely due to Malmquist bias for the limited co-add depth used in this analysis. Note that the poor agreement for faint hosts results in relatively small $\hat{S}_{\rm sim}$ errors because $\hat{S}_{\rm sim} \to 1$ (Eq. 11 and Fig. 2) as the underlying host becomes more faint, and therefore the range of possible $\hat{S}_{\rm sim}$ corrections is smaller.

Figure 7 shows data/simulation comparisons for the low-z sample. The $B_{\rm peak}$ distributions are forced to match because of the method for determining $E_{\rm spec}$. The comparisons for redshift, $E(B-V)$ and minimum $T_{\rm rest}$ show excellent agreement. The comparisons for maximum gap between observations (rest-frame) and maximum B-band SNR indicate a slight discrepancy. The SNR agreement is poorer compared to DES-SN because we do not have the observation information for the low-z sample, and thus rely on approximations (§6.1.1) to compute the noise in Eq. 11.

We have implemented SALT-II light curve fits on the simulations, and Fig. 7 of Brout et al. (2019b) shows data/simulation comparisons for the SALT-II parameters (m_B, x_1, c) and their uncertainties. The excellent agreement in these distributions adds confidence in our μ-bias predictions.

9 DISTANCE MODULUS BIAS VS. REDSHIFT

In one of our DES-SN3YR cosmology analyses (Brout et al. 2019b), we use the BBC method (Kessler & Scolnic 2017) in which μ-bias is characterized as a 5-dimensional function of $\{z, x_1, c, \alpha, \beta\}$. The first three parameters are observed, and

$\{\alpha, \beta\}$ are determined from the BBC fit. Here we illustrate μ-bias as a function of redshift for a variety of sub-samples, and also compare μ-bias for the two intrinsic scatter models (G10,C11) from §5.2. It is important to note that μ-bias is not a correction for the SN magnitude, but is a correction for fitted light curve parameters (describing the stretch, color and brightness) along with a correction for the impact of intrinsic scatter in which brighter events are preferentially selected in a magnitude-limited survey.

The true distance modulus is defined as $\mu_{\rm true}$, and the measured distance modulus (μ) is determined in the analysis from Tripp (1998),

$$\mu = -2.5\log(x_0) + \alpha x_1 - \beta c + \mathcal{M} , \qquad (18)$$

where $\{x_0, x_1, c\}$ are fitted SALT-II light-curve parameters, α and β are the standardization parameters, and $\mathcal{M}$ is an offset so that $\mu = \mu_{\rm true}$ when the true values of $\{x_0, x_1, c\}_{\rm true}$ are used in Eq. 18. The distance modulus bias is defined as μ-bias $\equiv \mu - \mu_{\rm true}$. The BBC method applies a μ-bias correction for each event, and determines the following parameters in a fit to the entire sample: $\alpha, \beta, \mathcal{M}$, and a weighted-average bias-corrected distance modulus in discrete redshift bins.

We implement the BBC procedure on a simulated DES-SN3YR data sample with 3×10^4 events after applying the cuts from §8. The μ-bias thus has contributions from the `DiffImg` trigger, spectroscopic selection, and analysis cuts. We use a large 'bias-correction' sample with 1.3×10^6 events after the same cuts. Samples are generated with both the G10 and C11 intrinsic scatter model, and the bias-correction sample with the correct intrinsic scatter model is used on the data; the effect of using the incorrect model is discussed in Brout et al. (2019b).

To account for a μ-bias dependence on α and β, we generate the bias-correction sample on a 2×2 grid of $\alpha \times \beta$ and use this grid for interpolation within the BBC fit. The grid values are $\alpha = \{0.10, 0.24\}$, $\beta_{\rm G10} = \{2.7, 3.5\}$, and $\beta_{\rm C11} = \{3.3, 4.3\}$.

The BBC-fitted values of α and β are un-biased within their 5% statistical uncertainties, and fitting with optional z-dependent slope parameters, $d\alpha/dz$ and $d\beta/dz$ are both consistent with zero. $\mathcal{M}$ does not contribute to μ-bias and therefore the μ-bias is caused by the fitted light curve parameters $\{x_0, x_1, c\}$. The μ-bias versus redshift from the BBC fit is shown in Figs. 8-9 for the low-z and DES-SN samples, respectively. The filled circles correspond to the G10 intrinsic scatter model, and open circles correspond to C11.

The average μ-bias (left panels) is zero at the lower end of the redshift range. At higher redshifts, μ-bias depends on the intrinsic scatter model, reaching ~ 0.05 mag at the high-redshift range. The middle and right panels of Figs. 8-9 show that μ-bias is much larger within restricted color ranges, reaching up to 0.4 mag for the reddest ($c > 0.06$) events. All panels show a μ-bias difference between the G10 and C11 models, and this difference is largely due to the different parent color populations (Scolnic et al. 2014a): the C11 color population has a sharp cut-off on the blue side, while the G10 population has a tail extending bluer than in the C11 model. These μ-bias differences, along with differences in fitted α and β, are incorporated into the systematic uncertainty in Brout et al. (2019b).

The large μ-bias for red events at higher redshift is because most of these events are intrinsically blue, which are
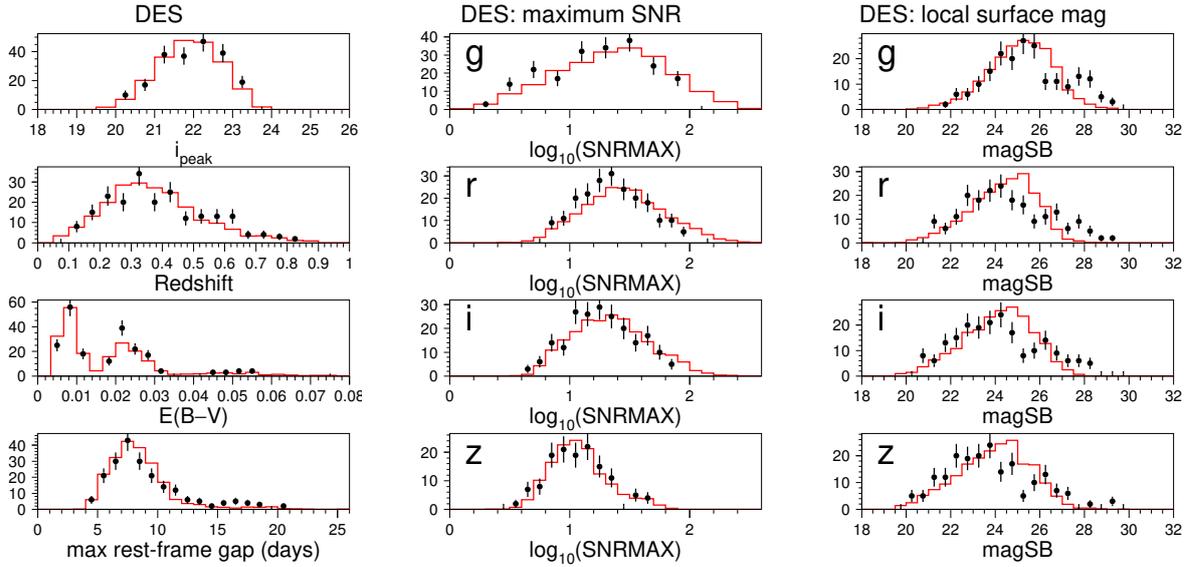
Figure 6. Comparison of data (black dots) and simulation with G10 scatter model (red histogram) for distributions in the DES-SN sample, where the simulation is scaled to have the same number of events as the data. Left column shows i_{peak}, CMB redshift, Galactic extinction, and maximum gap between observations (rest frame). Middle column shows log of maximum SNR in each band. Right column shows local surface mag in each band.
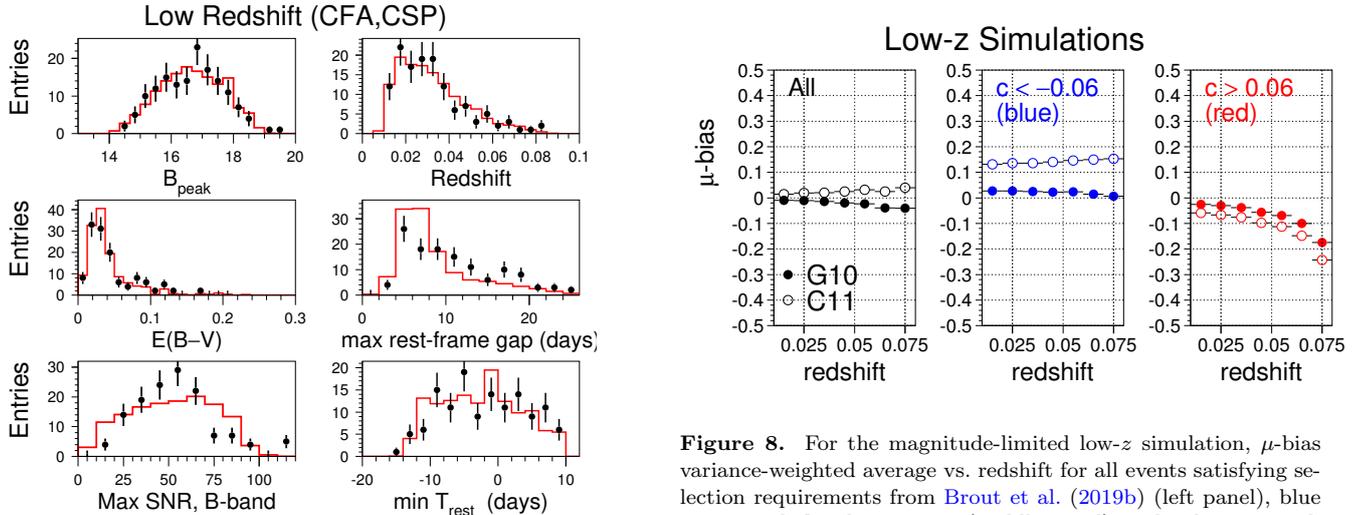

Figure 7. Data/simulation comparisons for distributions in the low-z sample, using the G10 intrinsic scatter model and magnitude-limited selection model.

Figure 8. For the magnitude-limited low-z simulation, μ-bias variance-weighted average vs. redshift for all events satisfying selection requirements from Brout et al. (2019b) (left panel), blue events with fitted $c < -0.06$ (middle panel), and red events with fitted $c > 0.06$ (right panel). Filled circles are with simulations using the G10 intrinsic scatter model; open circles are for the C11 model.

bright enough to be detected, but have poorly measured colors. Intrinsically red events are fainter and thus tend to be excluded at higher redshifts. To illustrate the size of the color uncertainties for the DES-SN sample, we computed the rms on measured color minus true color, rms(Δc), and the rms of the true color population, rms(c_{true}). The ratio is rms(Δc)/rms(c_{true}) ~ 0.5. Therefore the typical difference between measured and true color is 50% of the size of the intrinsic color distribution. For redshifts $z > 0.5$ this ratio increases to 0.7. A similar exercise with the stretch parameter results in similar ratios.

As described in §5.3, a new feature in the BBC method is to account for the μ-bias dependence on $\{\alpha, \beta\}$. This dependence is shown in Fig. 10 for DES-SN. Comparing simulations for $\alpha = 0.10$ and $\alpha = 0.24$ (nominal $\alpha \simeq 0.15$), the μ-bias difference reaches 0.03 mag at high redshift, and is similar for the two intrinsic scatter models (G10 and C11). The right panel in Fig. 10 shows the μ-bias difference with β values differing by ~ 1; the maximum μ-bias difference is 0.01 mag, and is similar for both intrinsic scatter models.

We end this section by illustrating the contributions to μ-bias for red events ($c > 0.06$) in the right panel of Fig. 9, where μ-bias reaches ~ 0.4 mag at the highest redshifts.
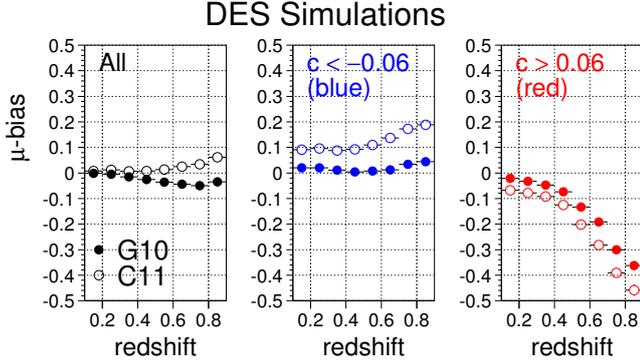
Figure 9. Same as Fig. 8, but for DES-SN.
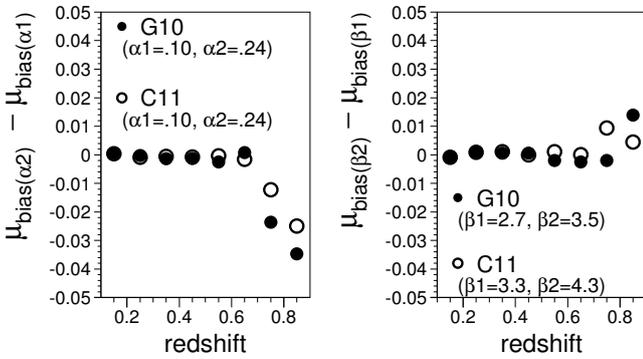
Figure 10. For the DES-SN sample, left panel shows μ-bias difference vs. redshift between $\alpha = 0.10$ and $\alpha = 0.24$. Right panel shows μ-bias difference between different β values: $\{2.7, 3.3\}$ for G10 intrinsic scatter model (filled circles), and $\{3.3, 4.3\}$ for C11 (open circles).

While high-redshift bias is often associated with Malmquist bias, we show that μ-bias is primarily associated with intrinsic scatter and light-curve fitting. We begin with an ideal DES-SN simulation that has no intrinsic scatter, and perform light-curve fits in which only the amplitude x_0 is floated while stretch and color (x_1, c) are assumed to be perfectly known. Defining $m_0 = -2.5 \log(x_0)$, μ-bias and m_0-bias are the same. The resulting μ-bias is shown by the dashed curve in Fig. 11a; this bias is only ~ 0.01 mag, a very small fraction of the μ-bias in Fig. 9. While there may be selection bias in the 2 detections contributing to the trigger (§7), the remaining few dozen epochs are not biased, and thus the majority of observations used to measure x_0 are un-biased.

The solid curve in Fig. 11a shows μ-bias with the G10 intrinsic scatter model, and still fitting only for x_0. In this case, μ-bias increases considerably to about 0.1 mag at the highest redshift, and is a result of the strong brightness correlations among epochs and passbands. While the true intrinsic scatter variations average to zero, magnitude-limited observations preferentially select positive brightness fluctuations, which lead to non-zero μ-bias.

Figure 11b shows the same simulations, but with light curve fits that float all three parameters (x_0, x_1, c). Compared with Fig. 11a, the μ-bias is much larger, mainly be-
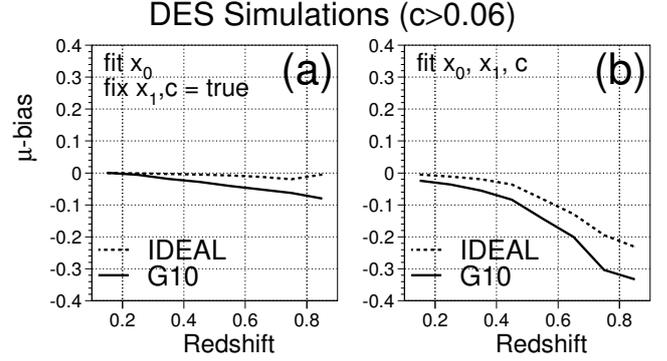
Figure 11. For the simulated DES-SN sample, (a) shows μ-bias vs. redshift for light curve fits that float x_0 only, while fixing stretch and color to their true values. (b) shows μ-bias vs. redshift for nominal light curve fits. Dashed line is for the ideal simulation defined as having no intrinsic scatter; solid line uses G10 intrinsic scatter model.

cause of the bias in fitted color. Although this μ-bias test is shown only for the the red events in Fig. 9, similar trends exist in all color ranges.

The statistical uncertainties on these μ-bias corrections are negligible. Systematic uncertainties in Brout et al. (2019b) are thus determined from changing input assumptions such as the color and stretch populations, model of intrinsic scatter, and the value of the flux-uncertainty scale, $\hat{S}_{\rm sim}$.

10 CONCLUSION

The SNANA simulation program has been under active development for a decade, and has been used in several cosmology analyses to accurately simulate SN Ia light curves and determine bias corrections for the distance moduli. This work focuses on simulated bias corrections for the DES-SN3YR sample, which combines spectroscopically confirmed SNe Ia from DES-SN and low-redshift samples. Files used to make these corrections are available at https://des.ncsa.illinois.edu/releases/sn.

The DES-SN simulation includes three categories of detailed modeling: (1) source model including the rest-frame SN Ia SED, cosmological dimming, weak lensing, peculiar velocity, and Galactic extinction, (2) noise model accounting for observation properties (PSF, sky noise, zero point), host galaxy, and information derived from 10,000 fake SN light curves overlaid on images and run through our image-processing pipelines, (3) trigger model of single-visit detections, candidate logic, and spectroscopic selection efficiency. The low-z sample, however, does not include observation properties, and thus approximations are used to simulate this sample. The quality of the simulation is illustrated by predicting observed distributions (Figs. 6-7), and bias corrections on the distance moduli are shown in Figs. 8-9.

The reliability of the bias corrections is only as good as the underlying assumptions in the simulation. To properly propagate bias correction uncertainties into systematic uncertainties on cosmological parameters, Brout et al. (2019a)

evaluate uncertainties for each of the 3 modeling categories above (source, noise, trigger). In addition to explicit assumptions such as those associated with the SALT-II model, one should always be aware of the implicit assumptions such as simulating SN properties (e.g., α, β) that are independent of redshift and host galaxy properties.

The simulations presented here are used to correct SN Ia distance biases in the DES-SN3YR sample (Brout et al. 2019b), and these bias-corrected distances are used to measure cosmological parameters (DES Collaboration et al. 2019). These simulations also serve as a starting point for the analysis of the full DES 5-year photometrically classified sample, which will be significantly larger than the DES-SN3YR sample.

APPENDIX A: ADDITIONAL SIMULATION FEATURES FOR FUTURE ANALYSIS

The focus of this work has been on simulating bias corrections and validation samples for the DES-SN3YR SN Ia cosmology analysis. Here we describe additional features of the SNANA simulation that have been developed for future work, but are beyond the current scope of the DES-SN3YR analysis. This future work includes extending the cosmology analysis to photometrically identified SNe Ia, more detailed systematics studies, determining the efficiency for Bayesian cosmology fitting methods (e.g., Rubin et al. 2015), determining the efficiency for SN rate studies, and optimizing future surveys. We end with a summary of missing features that would be useful to add for future analysis work.

A1   SED Time Series

The SALT-II light curve model, which is designed for SN Ia cosmology analyses, is a rather complex semi-analytical model. Most transient models, however, are much simpler. In addition to specialized SN Ia models,[10] the `SNANA` simulation works with arbitrary collections of SED time series. Each event can be generated from a random SED time series, or computed from parametric interpolation. For example, suppose a set of N_p parameters, $\vec{P} = \{p_1, p_2, ...p_{N_p}\}$, describes each SED time series. Each parameter (p_i) can be drawn from a Gaussian distribution (or asymmetric Gaussian) and a full covariance matrix to induce correlations. The SEDs on the parameter grid are interpolated to the generated $\vec{P}$.

Examples include CC simulations to model contamination in photometrically identified SN Ia samples (Kessler et al. 2010a; Rodney et al. 2012; Kessler & Scolnic 2017; Jones et al. 2017), and simulating Kilonovae (Barnes & Kasen 2013) to model the search efficiency (Soares-Santos et al. 2016; Doctor et al. 2017), and to predict discovery rates (Scolnic et al. 2018a).

An SED time series can also be useful for modeling SNe Ia. Examples include systematic studies on training the SALT-II model with simulated spectra (Hsiao et al. 2007; Mosher et al. 2014), and simulating spectra from SN Ia explosion models (Diemer et al. 2013; Kessler et al. 2013).

A2   Light Curve Library for Galactic Transients

Galactic transients can potentially contribute contamination in a photometrically identified SN Ia sample. To model galactic transients, the simulation reads a pre-computed 'light curve library' of transient magnitudes versus time. The light curves can be recurring or non-recurring. For recurring and long-lived non-recurring transients, the library specifies source magnitudes at epochs to use as templates for image-subtraction, and the simulation accounts for source signal in the templates. The subtracted fluxes can therefore be positive or negative. To detect negative fluxes with SNR < 0, there is an option to define the detection efficiency as a function of |SNR|. Each library light curve is overlaid on the survey time window, and overlapping observations in the cadence library are converted into a measured flux and uncertainty. Readers are cautioned that this model is relatively new, and has not yet been used in a publication.

A3   Characterization of Detection Efficiency

For the DES-SN3YR analysis, the DES detection efficiency was adequately characterized as a function of SNR. In the next cosmology analysis with a much larger photometric sample, we may need a more accurate description. In particular, we may need to characterize the efficiency of a machine learning (ML) requirement in `DiffImg` that was used to reject image-subtraction artifacts (Goldstein et al. 2015). The `SNANA` data file structure includes a 'PHOTPROB' entry for each epoch, which is intended to store information such as an ML score. The simulation can generate ML scores (between 0

---

and 1) based on an input probability map that depends on SNR and/or $m_{\rm SB}$. The input ML map should be generated from fakes processed through the same pipeline as the data. Since ML scores describe imaging data near the source, these scores are likely to be correlated among different epochs. A reduced correlation (0 to 1) can be provided to introduce ML correlations.

While we have been characterizing anomalous effects as a function of $m_{\rm SB}$, we have begun exploring the dependence on $m - m_{\rm SB}$, where m is the source magnitude. This source-to-galaxy flux ratio can be used to describe the detection efficiency or the ML map.

A4   Characterization of Flux-Uncertainty Scale

In §6.4 the flux-uncertainty scale, $\hat{S}_{\rm sim}$, was defined as a function of 1 parameter: $m_{\rm SB}$. In future work we plan to investigate if $\hat{S}_{\rm sim}$ depends on other parameters. The additional $\hat{S}_{\rm sim}$-dependent parameters in the simulation are: (1) SNR, (2) PSF, (3) MJD, (4) sky noise, (5) zero points, (6) galaxy magnitude, and (7) SN-host separation. Additional parameters, such as the source-to-galaxy flux ratio, can be added with minor code modifications.

A5   Rate Models

The following rate models can be used in the `SNANA` simulation:

- $R(z) = \alpha(1+z)^\beta$ with user-specified α, β. Multiple $R(z)$ functions can be defined, each in a different redshift range.
- $R(z) = A \cdot \int_\infty^z dz' {\rm SFR}(z') + B \cdot {\rm SFR}(z)$ where SFR is the star formation rate, A is the amplitude of the delayed component, and B is the amplitude of the prompt component (Scannapieco & Bildsten 2005; Mannucci et al. 2006).
- CC $R(z)$ measured with HST (Strolger et al. 2015).
- Star formation $R(z)$ from Madau & Dickinson (2014), where user defines $R(0)$.

A6   Redshift Dependent Input Parameters

Since redshift evolution is a concern in cosmology analyses, any simulation-input parameter can be given a redshift dependence: $P \to P + p_1 z + p_2 z^2 + p_3 z^3$, where P is a user-specified simulation parameter and $p_{1,2,3}$ are user-defined parameters. If a 3rd-order polynomial is not adequate, the simulation can read an explicit $P(z)$ map in arbitrary redshift bins.

A7   Population Parametrization

The SALT-II color and stretch populations are described by two asymmetric Gaussian profiles. The probability for color is defined as

$$P(c) \quad \propto \quad \exp[-(c - \bar{c})^2/2\sigma_+^2] \quad (c \geq \bar{c}) \qquad (A1)$$
$$P(c) \quad \propto \quad \exp[-(c - \bar{c})^2/2\sigma_-^2] \quad (c < \bar{c}) \qquad (A2)$$

and similarly for $P(x_1)$. A second asymmetric Gaussian can be added, as described in Appendix C of Scolnic et al. (2018b) for the low-z stretch distribution.

A8   Inhomogeneous Distributions

The DES-SN3YR simulations assume an isotropic and homogeneous universe on all distance scales because of the random selection of sky coordinates in the observation library (§6.1) and the random generation of redshifts. Large scale structure can be incorporated, but requires an external simulation to generate 3-dimensional (RA,DEC,z) galaxy locations. For each such galaxy, the RA, DEC and redshift are used to create an entry in the observation library.

Another application is to simulate transients corresponding to a posterior from a gravitational wave (GW) event found by the Large Interferometer Gravity Wave Observatory (Singer et al. 2016b,a, LIGO). Drawing random events from the posterior described by RA, DEC and distance, each event corresponds to an entry in the observation library.

A9   Host Galaxy Library Features

A host-galaxy library (HOSTLIB) was defined in §6.2 to model additional Poisson noise and the local surface brightness. Additional HOSTLIB features include:

• mis-matched host redshift model for photometrically identified sample (Jones et al. 2017),
• a weight map to assign SN magnitude offsets based on host-galaxy mass, or other properties such as specific star formation rate,
• photometric galaxy redshift (ZPHOT) and Gaussian uncertainty (ZPHOTERR), which must be computed externally from broadband filters,
• brightness distribution described with arbitrary sum of Sérsic profiles, each with its own index,
• correlation of host and SN properties by including SALT-II color and stretch for each HOSTLIB event.

A10   Generating Spectra

Ideally the modeling of spectroscopic selection would include an analysis of simulated spectra, but instead we empirically model this efficiency as a function of peak magnitude. To begin the effort on modeling spectroscopic selection, the SNANA simulation was enhanced to generate spectra for the WFIRST simulation study in Hounsell et al. (2018). Spectra are characterized by their SNR versus wavelength. They can be generated at specific dates in the observation library, or a random date can be selected in time windows with respect to peak brightness. This time-window can be specified in either the rest-frame or observer-frame, although the former is more difficult to carry out in practice. Spectral slices can also be integrated and stored as broadband fluxes.

Finally, a high-SNR (low-z) spectrum can be simulated at arbitrary redshift to examine the expected SNR degradation versus distance.

A11   Missing Features

We finish this section with a few features that are not included in the simulation, but might be useful in future analyses:

• peculiar velocity covariances (currently all v_{pec} are uncorrelated),
• galactic $E(B-V)$ covariance (currently all extinctions are uncorrelated),
• spectral PCA coefficients in the HOSTLIB to model host contamination in spectra,
• probability distribution for host-galaxy photometric redshifts (instead of Gaussian-error approximation),
• anomalous detection inefficiency from bright galaxies,
• weak lensing magnification model (§5.4) accounting for correlations between events with small angular separations.

APPENDIX B: AUTHOR AFFILIATIONS

[1] Department of Astronomy and Astrophysics, University of Chicago, Chicago, IL 60637, USA
[2] Kavli Institute for Cosmological Physics, University of Chicago, Chicago, IL 60637, USA
[3] Department of Physics and Astronomy, University of Pennsylvania, Philadelphia, PA 19104, USA
[4] School of Mathematics and Physics, University of Queensland, Brisbane, QLD 4072, Australia
[5] Lawrence Berkeley National Laboratory, 1 Cyclotron Road, Berkeley, CA 94720, USA
[6] The Research School of Astronomy and Astrophysics, Australian National University, ACT 2601, Australia
[7] Institute of Cosmology and Gravitation, University of Portsmouth, Portsmouth, PO1 3FX, UK
[8] ARC Centre of Excellence for All-sky Astrophysics (CAASTRO), Sydney, Australia
[9] School of Physics and Astronomy, University of Southampton, Southampton, SO17 1BJ, UK
[10] University of Copenhagen, Dark Cosmology Centre, Juliane Maries Vej 30, 2100 Copenhagen O
[11] Korea Astronomy and Space Science Institute, Yuseong-gu, Daejeon, 305-348, Korea
[12] Harvard-Smithsonian Center for Astrophysics, 60 Garden St., Cambridge, MA 02138, USA
[13] INAF, Astrophysical Observatory of Turin, I-10025 Pino Torinese, Italy
[14] Millennium Institute of Astrophysics and Department of Physics and Astronomy, Universidad Católica de Chile, Santiago, Chile
[15] South African Astronomical Observatory, P.O.Box 9, Observatory 7935, South Africa
[16] Space Telescope Science Institute, 3700 San Martin Drive, Baltimore, MD 21218, USA
[17] Department of Astronomy, University of California, Berkeley, CA 94720-3411, USA
[18] Miller Senior Fellow, Miller Institute for Basic Research in Science, University of California, Berkeley, CA 94720, USA
[19] Santa Cruz Institute for Particle Physics, Santa Cruz, CA 95064, USA
[20] Centre for Astrophysics & Supercomputing, Swinburne University of Technology, Victoria 3122, Australia
[21] Department of Physics, University of Namibia, 340 Mandume Ndemufayo Avenue, Pionierspark, Windhoek, Namibia
[22] Harvard-Smithsonian Center for Astrophysics, 60 Garden St., Cambridge, MA 02138,USA

[23] Gordon and Betty Moore Foundation, 1661 Page Mill Road, Palo Alto, CA 94304,USA

[24] Sydney Institute for Astronomy, School of Physics, A28, The University of Sydney, NSW 2006, Australia

[25] Institute of Astronomy and Kavli Institute for Cosmology, Madingley Road, Cambridge, CB3 0HA, UK

[26] National Center for Supercomputing Applications, 1205 West Clark St., Urbana, IL 61801, USA

[27] Institute of Astronomy, University of Cambridge, Madingley Road, Cambridge CB3 0HA, UK

[28] Division of Theoretical Astronomy, National Astronomical Observatory of Japan, 2-21-1 Osawa, Mitaka, Tokyo 181-8588, Japan

[29] Institute of Astronomy and Astrophysics, Academia Sinica, Taipei 10617, Taiwan

[30] Observatories of the Carnegie Institution for Science, 813 Santa Barbara St., Pasadena, CA 91101, USA

[31] Cerro Tololo Inter-American Observatory, National Optical Astronomy Observatory, Casilla 603, La Serena, Chile

[32] Fermi National Accelerator Laboratory, P. O. Box 500, Batavia, IL 60510, USA

[33] Kavli Institute for Cosmology, University of Cambridge, Madingley Road, Cambridge CB3 0HA, UK

[34] LSST, 933 North Cherry Avenue, Tucson, AZ 85721, USA

[35] CNRS, UMR 7095, Institut d'Astrophysique de Paris, F-75014, Paris, France

[36] Sorbonne Universités, UPMC Univ Paris 06, UMR 7095, Institut d'Astrophysique de Paris, F-75014, Paris, France

[37] Department of Physics & Astronomy, University College London, Gower Street, London, WC1E 6BT, UK

[38] Kavli Institute for Particle Astrophysics & Cosmology, P. O. Box 2450, Stanford University, Stanford, CA 94305, USA

[39] SLAC National Accelerator Laboratory, Menlo Park, CA 94025, USA

[40] Centro de Investigaciones Energéticas, Medioambientales y Tecnológicas (CIEMAT), Madrid, Spain

[41] Laboratório Interinstitucional de e-Astronomia - LIneA, Rua Gal. José Cristino 77, Rio de Janeiro, RJ - 20921-400, Brazil

[42] Department of Astronomy, University of Illinois at Urbana-Champaign, 1002 W. Green Street, Urbana, IL 61801, USA

[43] Institut de Física d'Altes Energies (IFAE), The Barcelona Institute of Science and Technology, Campus UAB, 08193 Bellaterra (Barcelona) Spain

[44] Institut d'Estudis Espacials de Catalunya (IEEC), 08034 Barcelona, Spain

[45] Institute of Space Sciences (ICE, CSIC), Campus UAB, Carrer de Can Magrans, s/n, 08193 Barcelona, Spain

[46] Observatório Nacional, Rua Gal. José Cristino 77, Rio de Janeiro, RJ - 20921-400, Brazil

[47] Department of Physics, IIT Hyderabad, Kandi, Telangana 502285, India

[48] Department of Astronomy/Steward Observatory, 933 North Cherry Avenue, Tucson, AZ 85721-0065, USA

[49] Jet Propulsion Laboratory, California Institute of Technology, 4800 Oak Grove Dr., Pasadena, CA 91109, USA

[50] Instituto de Fisica Teorica UAM/CSIC, Universidad Autonoma de Madrid, 28049 Madrid, Spain

[51] Department of Astronomy, University of Michigan, Ann Arbor, MI 48109, USA

[52] Department of Physics, University of Michigan, Ann Arbor, MI 48109, USA

[53] Department of Physics, ETH Zurich, Wolfgang-Pauli-Strasse 16, CH-8093 Zurich, Switzerland

[54] Center for Cosmology and Astro-Particle Physics, The Ohio State University, Columbus, OH 43210, USA

[55] Department of Physics, The Ohio State University, Columbus, OH 43210, USA

[56] Harvard-Smithsonian Center for Astrophysics, Cambridge, MA 02138, USA

[57] Australian Astronomical Optics, Macquarie University, North Ryde, NSW 2113, Australia

[58] Departamento de Física Matemática, Instituto de Física, Universidade de São Paulo, CP 66318, São Paulo, SP, 05314-970, Brazil

[59] George P. and Cynthia Woods Mitchell Institute for Fundamental Physics and Astronomy, and Department of Physics and Astronomy, Texas A&M University, College Station, TX 77843, USA

[60] Department of Astronomy, The Ohio State University, Columbus, OH 43210, USA

[61] Institució Catalana de Recerca i Estudis Avançats, E-08010 Barcelona, Spain

[62] Brandeis University, Physics Department, 415 South Street, Waltham MA 02453

[63] Instituto de Física Gleb Wataghin, Universidade Estadual de Campinas, 13083-859, Campinas, SP, Brazil

[64] Computer Science and Mathematics Division, Oak Ridge National Laboratory, Oak Ridge, TN 37831

REFERENCES

Astier P., Guy J., Regnault N., et al., 2006, A&A, 447, 31

Barnes J., Kasen D., 2013, ApJ, 775, 18

Bernstein J. P., Kessler R., Kuhlmann S., et al., 2012, ApJ, 753, 152

Betoule M., Kessler R., Guy J., et al., 2014, A&A, 568, A22

Brout D., Sako M., Scolnic D., et al., 2019a, ApJ, 874, 106

Brout D., Scolnic D., Kessler R., et al., 2019b, ApJ, 874, 150

Burns C. R., Stritzinger M., Phillips M. M., et al., 2011, AJ, 141, 19

Carretero J., Castander F. J., Gaztañaga E., Crocce M., Fosalba P., 2015, MNRAS, 447, 646

Chotard N., Gangler E., Aldering G., et al., 2011, A&A, 529, L4

Conley A., Guy J., Sullivan et al., 2011, ApJS, 192, 1

Contreras C., Hamuy M., Phillips M. M., et al., 2010, AJ, 139, 519

Crocce M., Castander F. J., Gaztañaga E., Fosalba P., Carretero J., 2015, MNRAS, 453, 1513

D'Andrea D., Smith M., Sullivan M., et al., 2018, ArXiv:1811.09565,

DES Collaboration et al., 2019, ApJ, 872, L30

Davis T. M., Hui L., Frieman J. A., et al., 2011, ApJ, 741, 67

Delgado F., Saha A., Chandrasekharan S., et al., 2014, in Modeling, Systems Engineering, and Project Management for Astronomy VI. p. 915015, doi:10.1117/12.2056898

Diehl H. T., Neilsen E., Gruendl R., et al., 2016, in Observatory Operations: Strategies, Processes, and Systems VI. p. 99101D, doi:10.1117/12.2233157

Diemer B., Kessler R., Graziani C., et al., 2013, ApJ, 773, 119

Doctor Z., Kessler R., Chen H. Y., et al., 2017, ApJ, 837, 57

Fitzpatrick E. L., 1999, PASP, 111, 63

Flaugher B., Diehl H. T., Honscheid K., et al., 2015, AJ, 150, 150

Folatelli G., Phillips M. M., Burns C. R., et al., 2010, AJ, 139, 120

Foreman-Mackey D., Hogg D. W., Lang D., Goodman J., 2013, PASP, 125, 306

Frieman J. A., Bassett B., Becker A., et al., 2008, AJ, 135, 338

Ganeshalingam M., Li W., Filippenko A. V., 2013, MNRAS, 433, 2240

Goldstein D. A., D'Andrea C. B., Fischer J. A., et al., 2015, AJ, 150, 82

Gupta R. R., Kuhlmann S., Kovacs E., et al., 2016, AJ, 152, 154

Guy J., Sullivan M., Conley A., et al., 2010, A&A, 523, A7

Hicken M., Challis P., Jha S., et al., 2009, ApJ, 700, 331

Hicken M., Challis P., Kirshner R. P., et al., 2012, ApJS, 200, 12

Hounsell R., Scolnic D., Foley R. J., et al., 2018, ApJ, 867, 23

Hsiao E. Y., Conley A., Howell D. A., et al., 2007, ApJ, 663, 1187

Jha S., Riess A. G., Kirshner R. P., 2007, ApJ, 659, 122

Jones D. O., Scolnic D. M., Riess A. G., et al., 2017, ApJ, 843, 6

Jones D. O., Scolnic D. M., Riess A. G., et al., 2018, ApJ, 857, 51

Kaiser N., Aussel H., Burke B. E., et al., 2002, in Tyson J. A., Wolff S., eds, Society of Photo-Optical Instrumentation Engineers (SPIE) Conference Series Vol. 4836, Survey and Other Telescope Technologies and Discoveries. pp 154–164, doi:10.1117/12.457365

Kessler R., Scolnic D., 2017, ApJ, 836, 56

Kessler R., Bernstein J. P., Cinabro D., et al., 2009a, PASP, 121, 1028

Kessler R., Becker A. C., Cinabro D., et al., 2009b, ApJS, 185, 32

Kessler R., Bassett B., Belov P., et al., 2010a, PASP, 122, 1415

Kessler R., Cinabro D., Bassett B., et al., 2010b, ApJ, 717, 40

Kessler R., Guy J., Marriner J., et al., 2013, ApJ, 764, 48

Kessler R., Marriner J., Childress M., et al., 2015, AJ, 150, 172

LSST Science Collaboration et al., 2009, arXiv:0912.0201,

Madau P., Dickinson M., 2014, ARA&A, 52, 415

Mannucci F., Della Valle M., Panagia N., 2006, MNRAS, 370, 773

Mosher J., Guy J., Kessler R., et al., 2014, ApJ, 793, 16

Perlmutter S., Alfdering G., Goldhaber G., et al., 1999, ApJ, 517, 565

Perrett K., Sullivan M., Conley A., et al., 2012, AJ, 144, 59

Rest A., Scolnic D., Foley R. J., et al., 2014, ApJ, 795, 44

Riess A. G., Filippenko A. V., Challis P., et al., 1998, AJ, 116, 1009

Rodney S. A., Riess A. G., Dahlen T., et al., 2012, ApJ, 746, 5

Rubin D., Aldering G., Barbary K., Boone K., Chappell G., et al., 2015, ApJ, 813, 137

Sako M., Bassett B., Becker A. C., et al., 2018, PASP, 130, 064002

Scannapieco E., Bildsten L., 2005, ApJ, 629, L85

Schlafly E. F., Finkbeiner D. P., 2011, ApJ, 737, 103

Schlegel D. J., Finkbeiner D. P., Davis M., 1998, ApJ, 500, 525

Scolnic D., Kessler R., 2016, ApJ, 822, L35

Scolnic D. M., Riess A. G., Foley R. J., et al., 2014a, ApJ, 780, 37

Scolnic D., Rest A., Riess A., et al., 2014b, ApJ, 795, 45

Scolnic D., Kessler R., Brout D., et al., 2018a, ApJ, 852, L3

Scolnic D. M., Jones D. O., Rest A., et al., 2018b, ApJ, 859, 101

Singer L. P., Chen H.-Y., Holz D. E., et al., 2016a, ApJS, 226, 10

Singer L. P., Chen H.-Y., Holz D. E., et al., 2016b, ApJ, 829, L15

Soares-Santos M., Kessler R., Berger E., et al., 2016, ApJ, 823, L33

Strolger L.-G., Dahlen T., Rodney S. A., et al., 2015, ApJ, 813, 93

Tripp R., 1998, A&A, 331, 815

This paper has been typeset from a TEX/LATEX file prepared by the author.